In situ monitoring of size distributions and characterization of nanoparticles during W ablation in N$_2$ atmosphere

L. Landström[a)]

The Ångström Laboratory, Department of Materials Chemistry, Uppsala University, Box 538, SE-751 21 Uppsala, Sweden

Zs. Márton

Department of General Physics and Laserspectroscopy, University of Pécs, H-7624 Pécs, Ifjúság útja 6., Hungary

N. Arnold

Department of Applied Physics, Johannes Kepler University, A-4040 Linz, Austria

H. Högberg

Department of Physics, Thin Film Physics Division, Linköping University, SE-581 83 Linköping

M. Boman

The Ångström Laboratory, Department of Materials Chemistry, Uppsala University, Box 538, SE-751 21 Uppsala, Sweden

P. Heszler[b)]

The Ångström Laboratory, Department of Solid State Physics, Uppsala University, Box 534, SE-751 21 Uppsala, Sweden

Nanoparticles were generated by pulsed laser ablation of tungsten in a N$_2$ ambient at atmospheric pressure. Size distributions and concentrations were monitored *in situ* versus laser fluence, repetition rate, and ablated spot size, by a differential mobility analyzer and a particle counter. The multishot ablation threshold was determined to be ~ 6 J/cm^2 for the laser used (ArF excimer, $\lambda = 193$ nm). Mostly small, nonlognormally, distributed particles (< 20 nm in diameter) were generated below the ablation threshold (ϕ_{th}), and the relative concentration of larger particulates (> 20 nm in diameter) increased above ϕ_{th}. Modeling of the temperature and ablated depth dependence on fluence showed that the formation of clusters below ϕ_{th} could not be assigned to a thermal process, but are connected to particle condensation from a photochemically desorbed thin layer. X-ray diffraction and x-ray photoelectron spectroscopy analysis performed on polydisperse nanoparticles revealed an amorphous phase of the particles, and the elemental composition was found to be WN$_{0.3}$. © *2003 American Institute of Physics.* [DOI: 10.1063/1.1587253]

I. INTRODUCTION

Research in nanomaterials and nanopowders with grain sizes less than ~ 100 nm is today one of the fastest growing fields within materials science. This increasing interest stems from the unique properties that these nanostructured materials exhibit, usually size dependent and well differing from the corresponding bulk.[1,2]

Nanoparticles and nanomaterials can be synthesized by various techniques, e.g., mechanical (ball-milling),[3] template-based,[4] sol–gel,[5] and gas phase synthesis [gas condensation, chemical vapor deposition (CVD) etc.].[6]

Pulsed laser ablation (PLA), whereby a material is evaporated by an intense laser pulse, is a well known technique for thin-film deposition as well as for the preparation of nanoparticles and nanomaterials.[7,8] The main advantage of PLA is the congruent (stoichiometric) material transport above the threshold fluence (ϕ_{th}), which is utilized for deposition of complex compounds such as high T_c superconductors. In addition, high melting point materials (e.g., C, W, and refractory ceramics) are easily deposited. Chemistry can also be performed if the ablation takes place in a reactive background gas.

Knowledge of the size distribution of the produced particles is crucial due to the size-dependent material properties, i.e., wide distributions may smear out the desired size effects. The use of a differential mobility analyzer (DMA) combined with a particle counter during nanoparticle production by PLA in an ambient gas allows *in situ* monitoring of the size distribution and concentration of the generated nanoparticles.[9–11] The high sensitivity of the condensation particle counter (CPC; 1 particle/cm^3), assuming that most of the ablated material condenses to nanoparticles, allows one to monitor the ablated depth in the range of $\sim 10^{-5}$ monolayer, which other techniques (e.g., atomic force and scanning electron microscopy) cannot perform. Therefore, the DMA+CPC system makes it possible to study the abla-

---

[a)]Author to whom correspondence should be addressed; electronic mail: lars.landstrom@mkem.uu.se

[b)]Also at: Research Group on Laser Physics of the Hungarian Academy of Sciences, Szeged, Box 406, H-6721, Hungary.
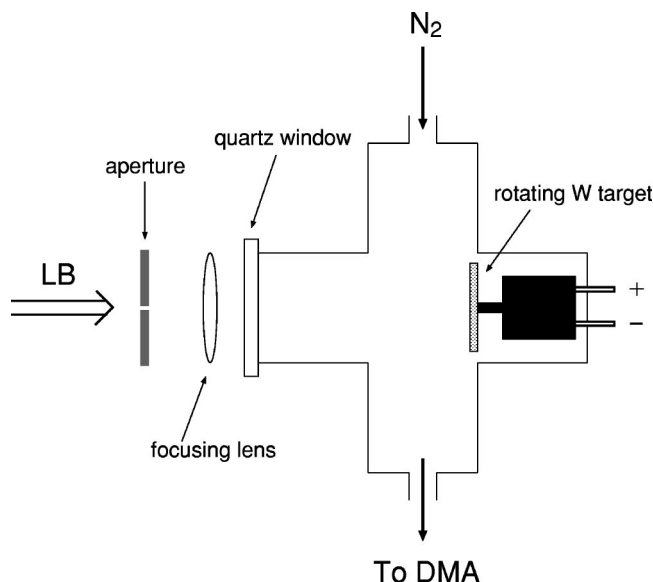
FIG. 1. Cross-sectional view of the ablation setup (LB denotes laser beam).

tion well below the ablation threshold, giving useful information about the ablation process.[12]

PLA of tungsten has been investigated for various different laser sources, e.g., Nd:YAG ($\lambda = 1064$ and 532 nm),[13–15] XeCl,[16] and sub-ps KrF.[17] Generation by Nd:YAG laser ablation and electron microscopy study of elemental nanoparticles of tungsten in an inert gas ambient (1.3–67 kPa) combined with a low-pressure DMA has also been reported.[10]

In this article, results on nanoparticle generation by ArF excimer PLA of tungsten in a N_2 ambient at atmospheric pressure is presented. The aim of this work is twofold. First, by exploiting the high detection sensitivity of the detection system (DMA+CPC), the ablated mass is monitored well below the ablation threshold. In addition, the temperature and ablated depth increase on laser fluence is modeled and compared with measured data. This gives further insight concerning the ablation, and it is shown that the ablation process has a clear nonthermal (photochemical) part beside the well-known thermal component. Second, the size distributions and particle concentrations are monitored as the experimental parameters are altered (spot size, laser fluence, and repetition rate), revealing the advantages and disadvantages of nanoparticle production by PLA. Deposited particles were also characterized by scanning electron microscopy (SEM), x-ray diffraction (XRD), and x-ray photoelectron spectroscopy (XPS).

II. EXPERIMENT

The experimental setup consisted of a stainless-steel cylindrical cross, see Fig. 1, with a quartz window and a rotating target on opposite sides. Perpendicular to the normal of the target was the gas inlet and outlet. The target was rotated with an angular speed of ~ 2 rad/s to avoid piercing. An ArF excimer laser [$\lambda = 193$ nm and laser pulse duration full width at half maximum (FWHM)$= 15$ ns] was focused onto the target by a fused silica lens ($f = 10$ cm), and the fluence and repetition rate were varied between $1.4 - 8.3$ J/cm^2 and 1–25

Hz, respectively. The ablated spot size was varied, at constant fluence (8 J/cm^2) and repetition rate (2 Hz), from 50 to 420 μm in diameter by changing the aperture in front of the focusing lens (Fig. 1). The DMA used was a TSI Inc. nano-DMA working at atmospheric pressure with the sheath flow and sample flow set at 4 slpm and 1 slpm, respectively. This instrument characterizes charged particles according to their electrical mobility, and the charging takes place prior to the DMA by a radioactive (^{85}Kr) source. A CPC from TSI Inc. analyzed the particle concentration. The flows used, combined with the size detection limit from the CPC, allowed a size window of 7 to 133 nm in diameter to be monitored for the aerosol particles in N_2. Nitrogen gas at atmospheric pressure was used as the ambient gas since its gas properties are similar to air (for which the DMA system was calibrated), and also because this DMA is limited to operate at atmospheric pressure. Measurements done with inert gases, such as argon, decreased the size window drastically due to the lower breakdown voltage of Ar compared to N_2 (or air). Furthermore, an impactor was applied before the DMA inlet in order to filter out particles above ~ 300 nm in diameter.

A polished polycrystalline W plate (purity $\sim 99.9\%$) was used as a target, and possible surface oxides and/or nitrides were removed by desorption before measurements by 15 min ablation (at 10 Hz repetition rate) below the ablation threshold for tungsten.

For deposition of the particles, a 0.5 mm diameter nozzle was used in an electrostatic precipitator (since the particles are charged) to increase the particle concentration per unit area. Both size-selected and polydisperse particles were deposited. The generated particles were collected on Si substrates for SEM, XRD, and XPS analysis.

III. RESULTS AND DISCUSSION

A. Ablation process

The ablation process can be divided in two different parts. (1) Above ϕ_{th}, the ablation plume consists of two components; the low yield desorptive part and the high yield (stoichiometric) forward peaked part. (2) Below ϕ_{th}, only the desorptive part can be found, and this part also exhibits a more sensitive angular dependence compared to the forward directed one.[7,8] At an elevated background gas pressure, particles are condensed within the plume and can be detected by means of a DMA and CPC.

The ablated mass and ablated depth dependence on laser fluence is depicted in Fig. 2. These values were obtained by assuming a density of 17.8 g/cm^3 of the generated particles (corresponding to W_2N)[18] and that all of the removed material condensed to clusters within the detection window (the net effect of these assumptions will most likely underestimate the amount of material removed). As the fluence is increased to ~ 6 J/cm^2, the increment of ablated mass is small, but an abrupt increase can be found at ~ 6 J/cm^2. Also note the linear increase on fluence at $\phi < 5$ J/cm^2 (see inset in Fig. 2). Since the ablation threshold (ϕ_{th}) is related to significant material removal, it is thus concluded that the multishot ablation threshold for tungsten is ~ 6 J/cm^2 for the laser source used ($\lambda = 193$ nm). This is also consistent with
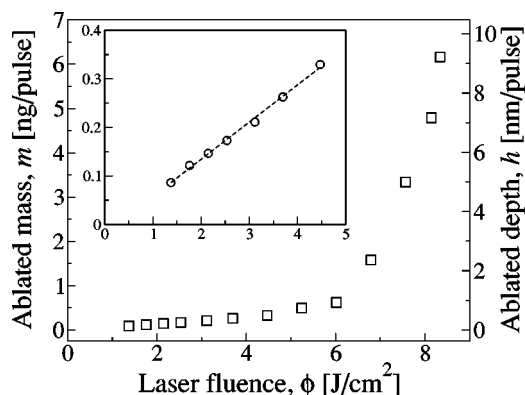
FIG. 2. Total mass (in 7–133 nm size window, left-hand side scale assuming bulk W_2N density of the particles) and ablated depth (right-hand side scale, assuming that all of the desorbed material forms nanoparticles) per laser pulse vs laser fluence. Repetition rate 2 Hz and spot diameter 210 μm. The ablation threshold (ϕ_{th}) can be seen at $\sim$6 J/cm. Inset shows a linear increase of ablation yield at fluences below $\sim$5 J/cm^2.

other observed values found in literature for ArF excimer ablated metals (see, e.g., Refs. 7 and 19 and references therein).

Interestingly, nanocluster formation was observed well below ϕ_{th}, down to $\sim$1.4 J/cm$^2 \approx \phi_{th}/4$, see Fig. 2. This is an indication that some nonthermal process may be involved. To investigate the possibility of a purely thermal mechanism, the temperature and amount of ablated material was estimated on the basis of thermal ablation model.[19]

As a first approximation, if material removal is purely thermal, then pronounced ablation by ns pulses is observed at temperatures somewhat above boiling temperatures ($\sim$5830 K for tungsten).[19] Alternatively, one can estimate which temperatures should be reached for tungsten in order to ablate, say 1 Å per pulse during the time $t < 100$ ns. These temperatures lie in the range of $\sim$4700 K.[20] Let us assume that observed threshold corresponds to either of these values, and that below the ablation threshold maximum temperature scales about linearly with fluence. Then, the temperatures reached for $\sim$1.4 J/cm^2 are about 1400–1600 K. The rate of

evaporation (sublimation) of tungsten is such, that only $\sim 10^{-16}$ Å of W per pulse can desorb at such temperatures. This is clearly not enough to provide material for cluster formation.

The conclusions of these simple estimations were also confirmed by more detailed calculations performed with the method of moments,[21] that includes temperature dependences of some material parameters (see Table I). These more detailed calculations will, of course, result in somewhat different absolute values (of ablated depth and temperature), compared to the earlier mentioned simple estimations. The laser intensity, $I(t)$, of a typical excimer laser pulse was approximated by the following smooth function[19]

$$I(t) = I_0 \frac{t}{\tau} \exp\left[-\frac{t}{\tau} \right], \tag{1}$$

where the laser fluence is given by $\phi = I_0 \tau$ and pulse width at half maximum $\tau_{FWHM} \approx 2.446\tau$.

To speed up the calculations, constant average values were taken for some of the parameters (see Table I). Steplike changes in material parameters at the melting point were smoothened over a finite temperature interval. This does not strongly affect the final result. One should add, that not all parameters for tungsten above the melting point are known. In particular, the evaporation rate given in Ref. 20 refers to solid state only (sublimation).

Special comment is in place with respect to the optical properties. High-temperature values of optical constants of tungsten at 193 nm have not been obtained by the authors. First, the Drude model was used to estimate high-temperature dielectric constant. Room-temperature plasma and electron collision frequency extracted from IR measurements are listed in Ref. 22. The electron collision frequency was assumed to increase proportionally to resistivity (taken from Ref. 23). Inserting this into Drude formulas for dielectric constant and Fresnel formulas for (normal incidence) absorptivity, resulted in a gradual increase in absorptivity up to 0.84 at temperatures above 5000 K. This naturally led to

TABLE I. Parameters used for thermal ablation calculations (T denotes the absolute temperature).

| Parameter	Symbol	Unit	Value
Melting temperature	T_m	(K)	3695
Boiling temperature	T_b	(K)	5828
Density	ρ	(g/cm^3)	19.3
Latent heat of fusion	ΔH_m	(J/g)	190
Latent heat of evaporation	ΔH_v	(kJ/g)	3.86
Evaporation rate	ν	(cm/s)	$\nu_0 \exp(-T_a/T)$
Pre-exponential factor	ν_0	(cm/s)	$2.65 \times 10^{10}/\sqrt{T}$
Activation temperature	T_a	(K)	92 702
Absorption coefficient	α	(cm^{-1})	2×10^6
Absorptivity	A		0.34
Thermal conductivity ($T < T_m$)	K	(W/cm K)	$1.24 \times 10^{-14}T^4 - 1.24 \times 10^{-10}T^3 + 4.9 \times 10^{-7}T^2 - 9.6 \times 10^{-4}T + 1.828$
Thermal conductivity ($T > T_m$)	K	(W/cm K)	$-1.06 \times 10^{-17}T^4 + 7.25 \times 10^{-13}T^3 - 1.97 \times 10^{-8}T^2 + 1.86 \times 10^{-4}T + 0.258$
Specific heat ($T < T_m$)	c	(J/g K)	$8.41 \times 10^{-16}T^4 - 3.91 \times 10^{-13}T^3 - 4.8 \times 10^{-9}T^2 + 2.8 \times 10^{-5}T + 0.1243$
Specific heat ($T > T_m$)	c	(J/g K)	0.1935
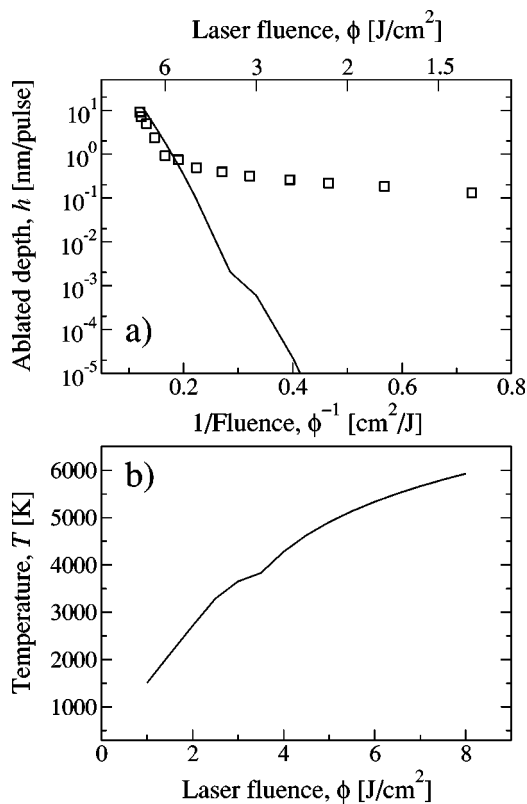
FIG. 3. (a) Arrhenius type of plot of calculated ablated depth per laser pulse. Solid line was obtained by the thermal ablation model and squares from experimental data, respectively. The lower axis represents inverse laser fluence $1/\phi$. For convenience, fluence values are indicated on the upper axis. Note the log scale on the depth scale. (b) Calculated maximal temperature of the ablated tungsten target.

FIG. 4. Typical size distributions obtained at 2 Hz repetition rate and ablated spot-size diameter 210 μm, above (solid line at 8.3 J/cm^2) and below ϕ_{th} (dotted line at 4.4 J/cm^2).

higher ablation rates than depicted in Fig. 3(a). (Curve not shown.)

But tungsten does not seem to be a Drude metal in the UV. The room-temperature data[24] indicated strong decrease in refractive index with wavelengths shorter than ~ 250 nm. Such behavior is impossible within the Drude model. Besides, Drude formulas predict unreasonably low α values ($\sim 2.5 \times 10^4$ cm^{-1}) at 193 nm even at room temperature. Most importantly, the available temperature dependent (300– 3600 K) data in the 250–350 nm range show a *decrease* of absorptivity with increasing temperature.[18,20] This effect can be associated with some interband transitions or with the anomalous skin effect,[22] though available data seem to produce too small values for the overall absorptivity. For the aforementioned reasons, reliable room-temperature values for the absorptivity and absorption coefficient were used over the whole range of temperatures.

The results from calculations (in ablated depth per pulse) are shown in Fig. 3(a) together with the experimental values from Fig. 2. One can see that at high fluences (above ~ 6 J/cm^2), the calculated results agree with an Arrhenius-type behavior found in experiments and a good correspondence between the slopes can be observed. It is also noted that the simulated ablated depths give larger values than the experimentally observed ones. This discrepancy can be explained by the fact that the values obtained from experiments were most likely underestimated (i.e., not all of the ablated
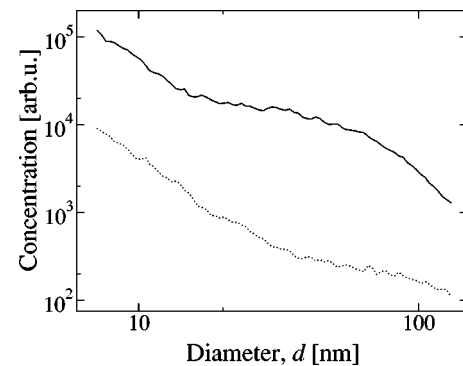
material forms particulates and particles outside the detection window were also generated). The estimated temperatures in this region are up to 6000 K, but the amount of ablated material is still too small to initiate noticeable deviation from an Arrhenius behavior, which occurs in the region of quasi-stationary ablation.[19]

Interesting divergence between the calculated and experimental results can be seen at low fluences. Cluster formation was observed already at ~ 1.4 J/cm^2 where estimated temperature is ~ 2000 K [see Fig. 3(b)]. As can be inferred from Fig. 3(a), the corresponding expected ablated depth is in the order of 10^{-16} nm. This means desorption of individual atoms only and this correlates well with the absolute thermal stability of tungsten at these temperatures. Melting, which can be seen as a small kink in calculated temperature and ablated depth plots (see Fig. 3), is expected at around 3 J/cm^2 only.

Even having in mind uncertainties in the absorptivity value, it seems highly unlikely that the clusters are produced thermally in the $1-2$ J/cm^2 fluence range. First, the amount of material that is thermally ablated at these fluences seems to be far too small. Second, the behavior of experimentally measured cluster yield as a function of laser fluence does not show Arrhenius behavior at all. In fact, the ablated mass increases linearly with laser fluence at $\phi < 5$ J/cm^2 (see inset in Fig. 2). This linearity is an indication that a single-photon photochemical process (i.e., nonthermal) is responsible for the material removal at low fluences, since the amount of tungsten that is desorbed is proportional to the number of incident photons.[19] Recalculating the fluence into the number of photons and comparing it with the amount of removed material from Fig. 2, a quantum yield of 0.002 atoms per photon was found in the low fluence range. However, for a photochemical process, one expects the extrapolated curve to pass through the origin, which is not the case (ablated mass equals zero at $\phi \approx 0.25$ J/cm^2, see inset in Fig. 2). This effect is again explained by the fact that clusters outside the detection limit are formed and that not all of the ablated material will condense into particles.

Typical size distributions are shown in Fig. 4 (above and below ϕ_{th}). Below ϕ_{th}, the distribution contains mostly small particles (< 20 nm in diameter) and increases slowly in mass concentration with increasing fluence (see Fig. 2). This
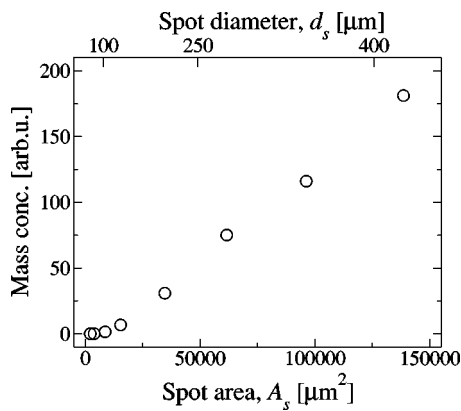
FIG. 5. Spot-size dependence on the ablated mass at repetition rate 2 Hz and fluence 8 J/cm^2.

FIG. 6. Repetition rate dependence on ablated mass at laser fluence 7 J/cm^2 and spot diameter 100 μm. Total mass concentration in 7–133 nm diameter size-window ($-\nabla-$) and for small particles (7–20 nm in diameter, $--\square--$). Inserted lines are a guide for the eyes.

small-sized contribution can be found at all fluences investigated, and it is noted that the shape of this distribution cannot be fitted to a lognormal distribution. Particles of larger sizes (>20 nm) increase in concentration relative to the smaller ones above ϕ_{th}, and as the fluence is increased this relative difference becomes more pronounced. If the shape of the distribution below ϕ_{th} is taken as the background and subtracted from the high fluence curve, a distribution (of the particles >20 nm) that resembles a lognormal is found. Since the appearance of the broad "peak" for larger particle sizes takes place above ϕ_{th}—combined with the fact that the small-sized contribution is present at all investigated fluences—it is thus concluded that the part at small sizes (<20 nm in diameter) emerges from the desorptive part and the peak at larger diameters from the forward directed real ablation. It also follows from this discussion (concerning the modeling of ablated depth and temperature) that this desorption exhibits a nonthermal characteristic.

The shape of both of these contributions to the size distribution remains unchanged as the fluence is increased, so these two different parts of the distribution are most likely separated in time (and/or space) during particle formation. Agglomeration and coalescence would otherwise most probably occur, resulting in a different shape of the size distribution. (Agglomeration and/or coalescence results in an increase in the concentration of the larger and decrease of the smaller mobility-diameter particles.)[25]

The ablated spot-area dependence on the ablated mass can be seen in Fig. 5. For larger spot areas (corresponding to diameters >100 μm), the mass is proportional to the area increase as expected, but at smaller spot areas (for diameters <100 μm), a deviation from a linear dependence is observed. As the spot diameter is decreased, the width of the angular distribution of the ablated material increases.[26] This effect explains the slight nonlinearity of the ablated mass at small spot areas, due to the decrease of oversaturation ratio as the angular distribution is widened, resulting in the formation of smaller particles outside the detection limit of the CPC. The shape of all recorded size distributions for the different ablated spot-area measurements were similar to the spectrum depicted in Fig. 4 (upper trace), i.e., above ϕ_{th}.
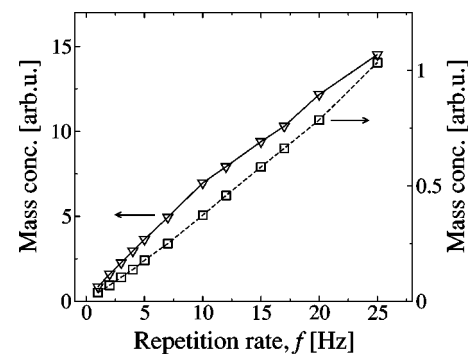
The mass concentration dependence on laser repetition rate is depicted in Fig. 6. Similar to the ablated spot-size dependence, the shape of all recorded distributions during repetition rate measurements resembled the size distribution shown in Fig. 4 (upper trace). For the small particles (7–20 nm in diameter), a linear dependence is observed in the measured frequency range (1–25 Hz), but for the total mass concentration (size window of 7–133 nm in diameter), a slight decrease of the slope can be seen at higher repetition rates. At elevated pressures, nanoparticle formation takes place in a ms (or less) timescale,[27] so as the repetition rate is increased, the interaction between the produced particles and following laser pulses becomes more significant. One effect of this interaction is the absorption of the incoming laser light, resulting in heating of the particles to temperatures ~ 3000 K or higher.[28] This heating induces evaporation of atoms from the nanoparticles and may lead to significant size decrease depending on the evaporation rate,[29] resulting in a reduction in the concentration of the small particles and, consequently, a change in shape of the size distribution. However, for the experimental parameters used, such a change could not be observed since a linear dependence for the smaller-sized (<20 nm in diameter) particles on the laser repetition rate was detected (see Fig. 6, dashed line). The slight decrease of the slope in total mass at high repetition rates can be explained by an attenuation of the laser light (e.g., by absorption and scattering) when high concentrations of particles are formed, resulting in a slightly less effective ablation process. In addition, the formation of larger particulates outside the observed size window at higher repetition rates would also decrease the total observed mass, but this effect does not seem to be significant since all of the observed distributions were similar in shape. (Only an increase in the concentration, independent of size, was observed as the repetition rate was increased.)

B. Characterization

SEM pictures of size-selected particles (40 nm in diameter) can be seen in Fig. 7. For short deposition times [Fig. 7(a)], the particles were found to be separated and one can observe the similarity in size. At longer deposition times [Fig. 7(b)], a high degree of agglomeration of the deposited particles was observed. Even though agglomeration occurs,
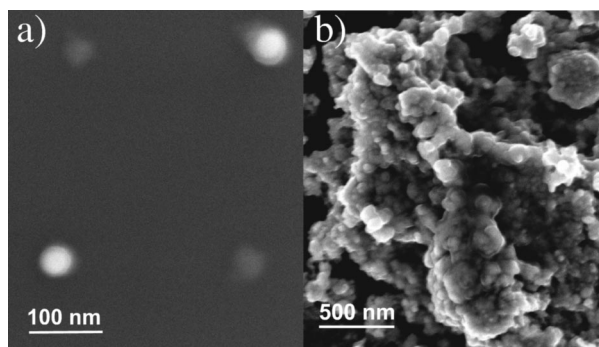
FIG. 7. SEM micrographs from size-selected (40 nm in diameter) particles produced above ϕ_{th} at different deposition times: (a) 5 min and (b) 45 min, respectively.

this deposition technique produces a high surface area material that can be used for, e.g., catalytic or sensor applications.

XPS analysis was performed on polydisperse particles passing only through the impactor. From the W $4f$ region [Fig. 8(a)], one can observe the W—W bonding from the $4f_{7/2}$ and $4f_{5/2}$ peaks at 31.0 and 33.2 eV, respectively. The relative intensities between the f peaks and the shoulders at higher binding energies also suggest that tungsten bonds to more electronegative elements (nitrogen and oxygen, in this case). Nitrogen and W—N bonding was also confirmed by the shift of the N $1s$ peak toward lower binding energy [~397.3 eV, Fig. 8(b)]. Taking the sensitivity factors into consideration, and relative intensities from the W $4f$ and N $1s$ peaks resulted in an elemental composition of $WN_{0.3}$. Small amounts of oxygen were also detected due to the rapid oxidation of tungsten as the samples were exposed to laboratory air.

The elemental composition reported here was obtained from particles generated above the threshold fluence only. Since it was shown that different processes govern the re-
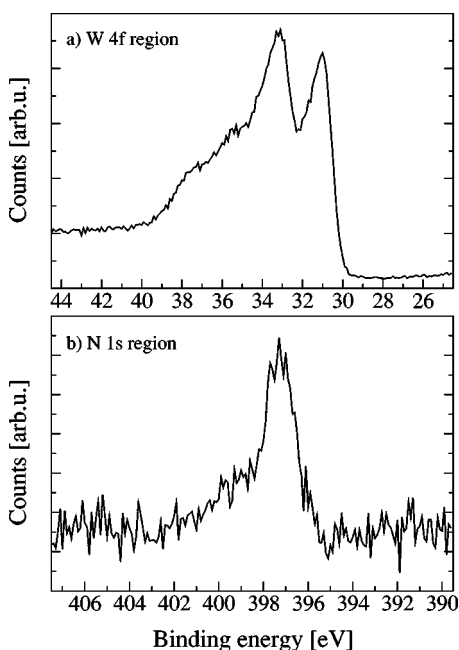

FIG. 8. XPS spectra from (a) W $4f$ and (b) N $1s$ regions, respectively.

moval of material above and below ϕ_{th}, one might expect a different composition of the nanoparticles formed below ϕ_{th} compared to above the same. Current work addressing this question is in progress for both tungsten and graphite ablation in a N_2 ambient, and will be reported elsewhere.[30]

Grazing incidence XRD of polydisperse samples (laser fluence 8 J/cm^2, spot size 420 μm, and repetition rate 2 Hz) revealed an amorphous phase of the particles, i.e., no distinct diffraction pattern could be obtained. This amorphous phase can be related to the small heat content and rapid quenching of the generated particles (see discussion next).

It is also noted that DMAs have been used for monitoring nanoparticles during the ablation of various materials using Nd:YAG lasers. For example, tungsten was ablated in He atmosphere at a pressure region of 1.3–67 kPa. A distribution similar to lognormal with a peak at ~10 nm in diameter was observed at a pressure of 40 kPa, and crystalline tungsten particles were formed at higher fluences.[10] A silicon target was ablated in an Ar atmosphere of 70–400 Torr, which resulted in a bimodal size distribution. As the ambient pressure and laser energy density increased, an enhancement of the concentration of larger particles was found.[31] Also, compound materials, such as CsI, have been monitored during Nd:YAG laser ablation of a cesium iodide rod in an argon atmosphere of 75–760 Torr. A bimodal lognormal distribution was observed at a laser fluence of ~1 J/cm^2 and 100 Torr ambient pressure. The smaller-sized particles decreased in concentration as the ambient pressure and laser fluence increased.[32]

In this study, it was shown that the size distribution of the nanoparticles formed from the quickly desorbed material was nonlognormal, but the condensation from the forward directed ablative part (above ϕ_{th}) yielded—most likely—a lognormal type with lower concentrations but larger diameters of the particles. At this stage of the research, no clear explanation for these results can be presented, but it is pointed out that the maximum fluence (8.3 J/cm^2) used in this work was only ~40% higher than the threshold fluence (~6 J/cm^2) and, consequently, the desorptive contribution to the total evaporated material becomes rather significant. This explains the unusual nonlognormal feature in our measured distributions.

Furthermore, no crystalline particles were formed in this present work. First, we note that crystalline tungsten nanoparticles could be generated if the particles were heated by subsequent laser pulses acting as postannealing with a laser fluence of ~160 mJ/cm^2 during low-pressure laser-assisted CVD (LCVD) studies.[28] Here, the laser fluence was estimated to be ~1 J/cm^2 in the condensation volume, i.e., a crystalline phase could be anticipated for the particles at the first glance. However, since the deposition for the materials characterization was performed at 2 Hz repetition rate, and taking into account the linear velocity of the gas flow (~1 cm/s), the plume size (~1−2 cm), and that the diameter of the laser beam was about 1.5 mm at a distance of 1−2 cm from the target surface; it follows that most of the condensed particles were not heated by subsequent laser pulses. Consequently, an amorphous phase could be expected, and was observed as well. In addition, it is also noted that the

atmospheric pressure ambient used during PLA measurements results in more than one order of magnitude higher cooling rate of the particles compared to the low-pressure LCVD experiments, and that may also effect the crystallinity of the deposited material. Finally, the fraction of W—N bonding, as confirmed by XPS, will most probably also interfere with the crystallization process.

IV. SUMMARY

Amorphous $WN_{0.3}$ nanoparticles were generated by pulsed excimer ablation of tungsten in a N_2 ambient at atmospheric pressure and, most likely, the limited thermal budget of the produced particles resulted in the amorphous phase. Size distributions and concentrations were monitored *in situ* by a DMA in combination with a CPC with respect to different laser parameters and spot sizes. Ablated mass dependence on the laser fluence in the investigated size window (7–133 nm in diameter) gave information about the multishot ablation threshold at $\lambda = 193$ nm (~ 6 J/cm^2). In addition, different stages of material removal could be monitored. It was concluded that the fast desorptive part for which a thermal process for material removal was ruled out and the "real" ablation (above ϕ_{th}, that could be modeled by thermal evaporation) gave rise to different types of size distributions, and that the two stages were most likely separated in time and/or space.

The size distribution of the small-sized particles could not be assigned to a lognormal type, which is often encountered during nanoparticle production by other techniques. As for the larger particles (>20 nm) that increase in concentration above ϕ_{th} a distribution that resembles a lognormal was found. Deviation from a linear relation of the ablated mass versus spot-size dependence could be observed for small spot sizes (diameters <100 μm), and explained by a widening of the angular distribution of the ablated material. A slight deviation from a linear relation of the total mass versus laser repetition rate dependence could be seen, reasoned by an attenuation of the laser by the formed nanoparticles at higher repetition rates.

Importantly, concerning practical consequences, it has been shown that high concentrations of small nanoparticles (<20 nm in diameter) are formed below the ablation threshold during PLA of tungsten at atmospheric pressure. In nanotechnology, it is usually these small particles that are desirable. Thus, to increase the yield, a fluence, somewhat below ϕ_{th}, large spot size and high repetition rate, is to be preferred.

ACKNOWLEDGMENTS

[1] H. Gleiter, Acta Mater. **48**, 1 (2000).
[2] A. S. Edelstein, J. S. Murday, and B. B. Rath, Prog. Mater. Sci. **42**, 5 (1997).
[3] J. Eckert, J. C. Holzer, I. C. E. Krill, and W. L. Johnson, J. Mater. Res. **7**, 1751 (1992).
[4] A. Huczko, Appl. Phys. A: Mater. Sci. Process. **70**, 365 (2000).
[5] C. J. Brinker and G. W. Scherer, Sol–Gel Science (Academic, Boston, 1990).
[6] H. Hahn, Nanostruct. Mater. **9**, 3 (1997).
[7] D. B. Chrisey and E. G. K. Hubler, *Pulsed Laser Deposition of Thin Films* (Wiley, New York, 1994).
[8] D. H. Lowndes, D. B. Geohegan, A. A. Puretzky, D. P. Norton, and C. M. Rouleau, Science **273**, 898 (1996).
[9] R. R. Whitlock and G. M. Frick, J. Mater. Res. **9**, 2868 (1994).
[10] Y. Kawakami, T. Seto, and E. Ozawa, Appl. Phys. A: Mater. Sci. Process. **69**, 249 (1999).
[11] T. Makino, N. Suzuki, Y. Yamada, T. Yoshida, T. Seto, and N. Aya, Appl. Phys. A: Mater. Sci. Process. **69**, 243 (1999).
[12] Z. Márton, L. Landström, and P. Heszler (unpublished).
[13] H. Schwarz and H. A. Tourtellotte, J. Vac. Sci. Technol. **6**, 373 (1969).
[14] J. K. Kliwer, J. Appl. Phys. **44**, 490 (1973).
[15] J. Rothman, D. Givord, and C. Meyer, J. Magn. Magn. Mater. **165**, 202 (1997).
[16] V. P. Ageev, A. D. Akhsakhalyan, S. V. Gaponov, A. A. Gorbunov, V. I. Konov, and V. I. Luchin, Sov. Phys. Tech. Phys. **33**, 562 (1988).
[17] S. Preuss, A. Demchuk, and M. Stuke, Appl. Phys. A: Mater. Sci. Process. **61**, 33 (1995).
[18] *CRC Handbook of Chemistry and Physics*, edited by D. R. Lide (CRC Press, Boca Raton, 1990).
[19] D. Bäuerle, *Laser Processing and Chemistry*, 3rd ed. (Springer, Berlin, 2000).
[20] *American Institute of Physics Handbook*, edited by D. E. Gray (McGraw–Hill, New York, 1972).
[21] N. Arnold, B. Luk'yanchuk, and N. Bityurin, Appl. Surf. Sci. **127**, 184 (1998).
[22] A. M. Prokhorov, V. I. Konov, I. Ursu, and I. N. Mihailescu, *Laser Heating of Metals* (Hilger, Bristol, 1990).
[23] http://www.jahm.com/pages/onlinedemo.html
[24] *Handbook of Optical Constants of Solids*, edited by E. D. Palik (Academic, Orlando, 1985).
[25] D. L. Swift and S. K. Friedlander, J. Colloid Sci. **19**, 621 (1964).
[26] A. D. Akhsakhalyan, S. V. Gaponov, V. I. Luchin, and A. P. Chirimanov, Sov. Phys. Tech. Phys. **33**, 1146 (1988).
[27] D. B. Geohegan, A. A. Puretzky, and G. Duscher, Appl. Phys. Lett. **72**, 2987 (1998).
[28] P. Heszler, K. Elihn, L. Landström, and M. Boman, Smart Mater. Struct. **11**, 631 (2002).
[29] Z. Márton, L. Landström, M. Boman, and P. Heszler, Mater. Sci. Eng., C **23**, 225 (2003).
[30] L. Landström, H. Högberg, M. Boman, and P. Heszler (unpublished).
[31] K. S. Seol, R. P. Camata, and K. Takeuchi, J. Aerosol Sci. **30**, S467 (1999).
[32] R. P. Camata, M. Hirasawa, K. Okuyama, and K. Takeuchi, J. Aerosol Sci. **31**, 391 (2000).